Supporting Information

Veesler et al. 10.1073/pnas.1300601110

SI Materials and Methods

Virus Production. *Sulfolobus solfataricus* strain 2-2-12 cultures were infected with *Sulfolobus* turreted icosahedral virus (STIV) as previously described with some modification (1). *Sulfolobus* cells were grown from a glycerol stock in Medium 182 (2 g/L yeast extract, 23 mM KH_2PO_4, 19 mM $(NH_4)_2SO_4$, 1 mM $MgSO_4 \times 7H_2O$, 2 mM $CaCl_2 \times 2H_2O$) at pH 3.5. The cultures were passed twice to Medium 182 at pH 3.5 and once to Medium 182 at pH 2.5. When the optical density at 650 nm reached 0.2, the cells were infected with STIV at a multiplicity of infection (MOI) of 2 and incubated for 40 h before viruses were released from lysed cells. Virus particles were collected from the culture medium after removal of cellular debris via centrifugation. The supernatant was filtered through a vacuum-driven filtration system (Steritop; Millipore) and concentrated with centrifugation filter units with a 100-kDa cutoff (Amicon Ultra-100; Millipore). The concentrated supernatant was applied to a step density gradient with 23% and 38% (wt/vol) Cs_2SO_4 in Buffer 182 (23 mM KH_2PO_4, 19 mM $(NH_4)_2SO_4$, 1 mM $MgSO_4 \times 7H_2O$, 2 mM $CaCl_2 \times 2H_2O$) pH 3.2. The samples were centrifuged at 40,000 rpm for 4 h using a Beckman Coulter SW41 Ti rotor. The viral particles were recovered from the gradients and dialyzed against Buffer 182.

Electron Microscopy Data Collection. Frozen hydrated STIV virions were prepared using C-flat holey carbon grids (CF-2/2–4C, Protochips). Briefly, 3 μL of purified viruses were applied on the grids and manually blotted with filter paper before plunge freezing in liquid ethane using a homemade device. Samples were then transferred and stored in liquid nitrogen. Images were acquired with a FEI Titan Krios electron microscope operating at 300 kV at liquid nitrogen temperature with a calibrated magnification of 102,189× and a dose of 15–18 $e^-/Å^2$ using a FEI Falcon direct electron detector. About 900 micrographs were collected with under-focus values covering 0.8–2.5 μm.

Electron Microscopy Data Processing. Particles were automatically picked using FindEM (2) integrated into the Appion pipeline (3) before visual inspection to remove junk picks, overlapping particles, or particles being on the grid carbon. Capsids were then extracted using a box size of 1024 pixels at full resolution yielding a stack of 9,371 particle images. The parameters of the microscope contrast transfer function were estimated using CTFind3 (4) for each micrograph. A systematic search of particle image orientation was performed with Frealign (5) using the previously reported STIV reconstruction (6) low-pass filtered at 50 Å. We then carried out a local angular and positional refinement in Frealign while always limiting to 10 Å the resolution of the data included to avoid bias in the Fourier shell correlation (FSC) at higher resolution. The resolution of the obtained map was determined by using the FSC, calculated between two reconstructions each containing half of the data, at a cutoff of 0.143 (7). A negative temperature factor of 400 $Å^2$ was applied to the final reconstruction with the software Bfactor (http://emlab.rose2.brandeis.edu/bfactor).

Expression, Purification, and Crystallization of the A223 C-Terminal Domain. Nucleotides encoding residues 64–223 of an A223 Leu208Met variant along with a C-terminal His_6-tag were cloned into the pDEST14 (Invitrogen) expression vector. The protein was expressed in BL21-CodonPlus (DE3) RIL *Escherichia coli* using ZYP-5025 autoinduction medium (8). Cell pellets were resuspended in lysis buffer [20 mM Tris·HCl pH 8.0, 400 mM NaCl, and 0.1 mM phenylmethylsulfonylfluoride at 5–6 mL/g of wet cell pellet. The cells were lysed using a French press, and the lysate was heat treated at 65 °C for 25 min. The cleared lysate was then applied to a HIS-select nickel affinity resin, washed with 10 column volumes of wash buffer (lysis buffer with 20 mM imidazole pH 8.0) and eluted in elution buffer (20 mM Tris·HCl pH 8.0, 50 mM NaCl, and 200 mM imidazole). The eluted protein was applied to a Superdex 75 gel filtration column equilibrated with 10 mM Tris·HCl pH 8.0 and 50 mM NaCl. The purified protein was then concentrated by centrifugal filtration to 6 mg/mL Protein concentrations were determined by Bradford assay, using BSA as a standard.

Structure Determination of the A223 C-Terminal Domain. The Leu208Met A223 C-terminal domain variant was crystallized by hanging drop vapor diffusion, using 2 μL of protein and 1 μL of the well solution [0.1 M sodium citrate tribasic dihydrate pH 5.6, 10–15% (vol/vol) 2-propanol and 5–10% (wt/vol) polyethylene glycol 4,000] in each drop. Crystals were flash-frozen in liquid nitrogen before data collection. Crystals were also buffer exchanged into 0.1 M Mes pH 6.0, 15% isopropanol, and 5% polyethylene glycol 4,000 and soaked in 10 mM di-μ-iodobis(ethylenediamine)diplatinum (II) nitrate (Hampton Research) for 8–24 h and flash frozen for phase determination. All data were collected at SSRL beamline 9–2. The data were integrated, scaled, and reduced in space group $P3_22$ (Table S2), using HKL-2000 (9). Phases were determined by multiwavelength anomalous diffraction using data collected at the Pt LIII edge. Platinum positions and initial phases were determined with SOLVE (10). RESOLVE (11, 12) was used for density modification and initial model-building, followed by iterative model building and refinement with COOT (13) and REFMAC (14), using TLS groups chosen by the TLS motion determination server (15–17) and the Pt-free data set. Structure geometry (Table S3) was validated with MOLPROBITY (18) and deposited in the Protein Data Bank (PDB ID code 4IL7).

Model Building into the STIV Reconstruction. The B345 coat subunit X-ray structure (19) was initially rigid-body fit into the reconstruction using UCSF Chimera (20) to generate the five trimeric capsomers of the icosahedral asymmetric unit. Therefore, we refined the position of the polypeptide chains by rigid-body fitting with the Coot software (13) before manually adjusting the coordinates into the density along with real-space refinement. We built the A223 penton base protein until residue 138 directly into the density and fit the C-terminal domain X-ray structure (residue 138–222) to complete the model. The A55 membrane protein model was also built de novo into the cryoEM density, and the transmembrane helix was specifically modeled using a reconstruction sharpened with a negative temperature factor of 100 $Å^2$. We introduced the C381 turret protein X-ray structure into the cryoEM map by rigid-body fitting before adjusting manually the side chains interacting with the A223 penton base domain along with real-space refinement in Coot. Reciprocal space refinement of the atomic coordinates was carried out using the CNS software with strict noncrystallographic symmetry constraints and the maximum likelihood target using amplitudes and phase probability distribution (mlhl) target function (21). Electrostatics calculations were performed with pdb2pqr (22) and APBS (23) at 80 °C, pH 3.0 and 0.15 M NaCl. Structure analysis and interpretation were assisted by the DALI (24) and PISA (25) servers.

1. Maaty WSA, et al. (2006) Characterization of the archaeal thermophile Sulfolobus turreted icosahedral virus validates an evolutionary link among double-stranded DNA viruses from all domains of life. *J Virol* 80(15):7625–7635.
2. Roseman AM (2004) FindEM—a fast, efficient program for automatic selection of particles from electron micrographs. *J Struct Biol* 145(1-2):91–99.
3. Lander GC, et al. (2009) Appion: An integrated, database-driven pipeline to facilitate EM image processing. *J Struct Biol* 166(1):95–102.
4. Mindell JA, Grigorieff N (2003) Accurate determination of local defocus and specimen tilt in electron microscopy. *J Struct Biol* 142(3):334–347.
5. Grigorieff N (2007) FREALIGN: High-resolution refinement of single particle structures. *J Struct Biol* 157(1):117–125.
6. Khayat R, Fu C-Y, Ortmann AC, Young MJ, Johnson JE (2010) The architecture and chemical stability of the archaeal Sulfolobus turreted icosahedral virus. *J Virol* 84(18): 9575–9583.
7. Rosenthal PB, Henderson R (2003) Optimal determination of particle orientation, absolute hand, and contrast loss in single-particle electron cryomicroscopy. *J Mol Biol* 333(4):721–745.
8. Studier FW (2005) Protein production by auto-induction in high density shaking cultures. *Protein Expr Purif* 41(1):207–234.
9. Otwinowski Z, Minor W (1997) Processing of X-ray diffraction data collected in the oscillation mode. Methods Enzymol 276:307–326.
10. Terwilliger TC, Berendzen J (1999) Automated MAD and MIR structure solution. *Acta Crystallogr D Biol Crystallogr* 55(Pt 4):849–861.
11. Terwilliger TC (2000) Maximum-likelihood density modification. *Acta Crystallogr D Biol Crystallogr* 56(Pt 8):965–972.
12. Terwilliger TC (2003) Automated main-chain model building by template matching and iterative fragment extension. *Acta Crystallogr D Biol Crystallogr* 59(Pt 1):38–44.
13. Emsley P, Lohkamp B, Scott WG, Cowtan K (2010) Features and development of Coot. *Acta Crystallogr D Biol Crystallogr* 66(Pt 4):486–501.
14. Murshudov GN, Vagin AA, Dodson EJ (1997) Refinement of macromolecular structures by the maximum-likelihood method. *Acta Crystallogr D Biol Crystallogr* 53(Pt 3):240–255.
15. Winn MD, Murshudov GN, Papiz MZ (2003) Macromolecular TLS refinement in REFMAC at moderate resolutions. *Methods Enzymol* 374:300–321.
16. Painter J, Merritt EA (2006) TLSMD web server for the generation of multi-group TLS models. *J Appl Cryst* 39:109–111.
17. Painter J, Merritt EA (2006) Optimal description of a protein structure in terms of multiple groups undergoing TLS motion. *Acta Crystallogr D Biol Crystallogr* 62(Pt 4): 439–450.
18. Chen VB, et al. (2010) MolProbity: All-atom structure validation for macromolecular crystallography. *Acta Crystallogr D Biol Crystallogr* 66(Pt 1):12–21.
19. Khayat R, et al. (2005) Structure of an archaeal virus capsid protein reveals a common ancestry to eukaryotic and bacterial viruses. *Proc Natl Acad Sci USA* 102 (52):18944–18949.
20. Goddard TD, Huang CC, Ferrin TE (2007) Visualizing density maps with UCSF Chimera. *J Struct Biol* 157(1):281–287.
21. Brunger AT (2007) Version 1.2 of the Crystallography and NMR system. *Nat Protoc* 2(11):2728–2733.
22. Dolinsky TJ, et al. (2007) PDB2PQR: Expanding and upgrading automated preparation of biomolecular structures for molecular simulations. *Nucleic Acids Res* 35(Web Server issue):W522–W525.
23. Baker NA, Sept D, Joseph S, Holst MJ, McCammon JA (2001) Electrostatics of nanosystems: Application to microtubules and the ribosome. *Proc Natl Acad Sci USA* 98(18):10037–10041.
24. Holm L, Rosenström P (2010) Dali server: Conservation mapping in 3D. *Nucleic Acids Res* 38(Web Server issue):W545–W549.
25. Krissinel E, Henrick K (2007) Inference of macromolecular assemblies from crystalline state. *J Mol Biol* 372(3):774–797.

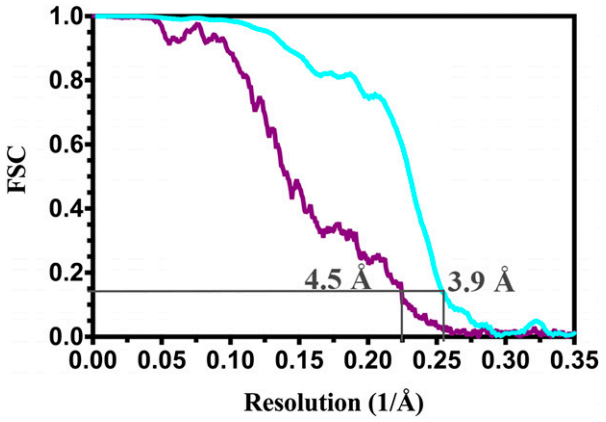

Fig. S1. FSC of the STIV reconstruction. The curves correspond to the FSC for the entire virus reconstruction (purple) and the B345 coat subunit region only (light blue). The resolution has been estimated using the 0.143 criterion to 4.5 Å and 3.9 Å for the whole reconstruction and B345, respectively.

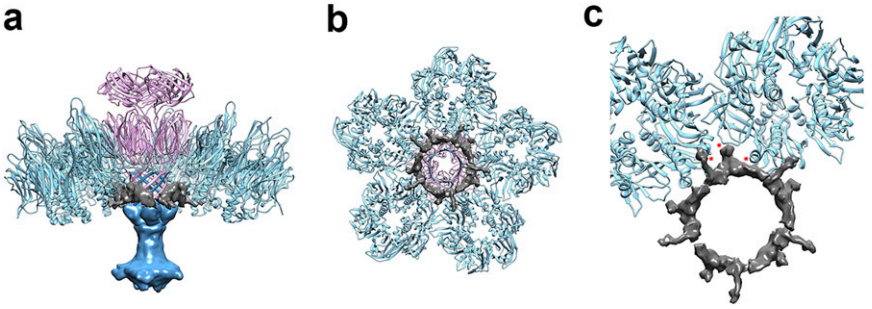

Fig. S2. The cement protein seals the interactions at each vertex complex. (*A*) A cement protein pentamer (dark gray) is bridging the bottom region of the B345 coat subunits with the β-pore by forming a ring around this latter. Only the extramembranous region of the A55 membrane protein is represented. One of the five B345 capsomers surrounding the A223 pentamer has been removed for clarity. (*B*) The cement protein pentamer viewed from the virion interior along an icosahedral fivefold axis. Only the N-terminal β-strand of A55 (contributing to the β-pore) is displayed. (*C*) Blow-up view of the interactions established between a single cement protein and two neighboring B345 coat subunits belonging to two icosahedral asymmetric units (indicated by red stars). The color code is the same as in Fig. 1.

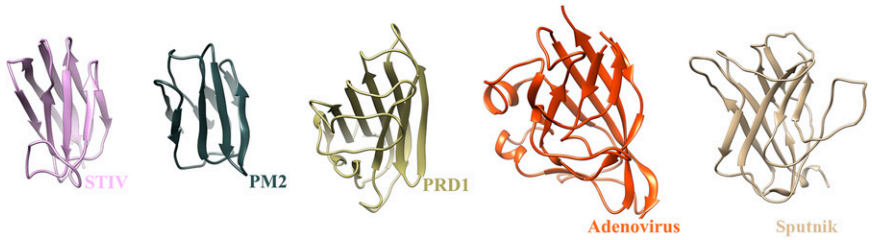

Fig. S3. Conservation of the penton base protein fold among viruses infecting the three kingdoms of life. The penton base domain of STIV (A223, light pink), PM2 (dark slate gray), PRD1 (khaki), Adenovirus (orange), and Sputnik (light brown) are shown in ribbon representation and with an equivalent orientation.

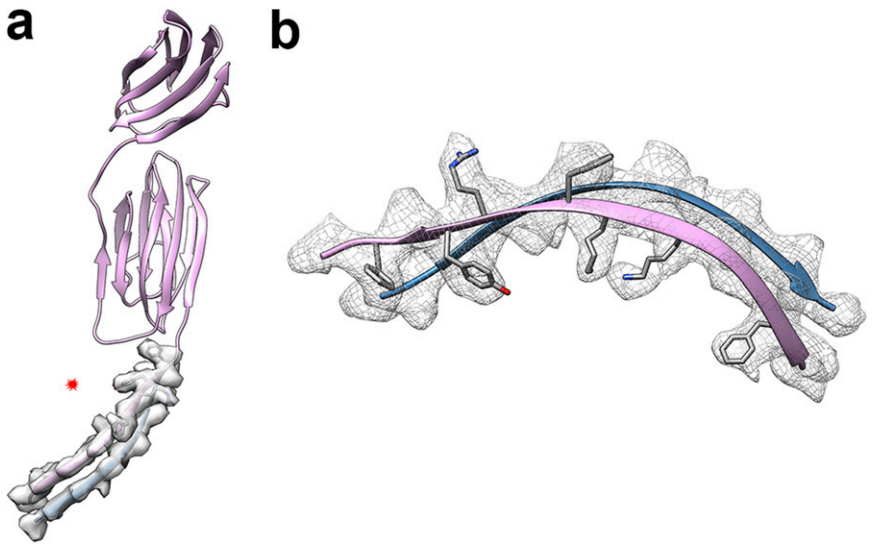

Fig. S4. Architecture of the β-pore. (*A*) One A223 monomer (light pink) is represented along with the adjacent A55 N-terminal β-strand (steel blue) belonging to the same icosahedral asymmetric unit. The cryoEM density corresponding to these two β-strands is also displayed. (*B*) Blow-up view of the two strands displayed in *A* within the cryoEM density (from the point of view annotated with a star). The side chains of the aromatic and bulky residues present in the A223 N-terminal region are displayed.

Table S1. Conserved interactions between B345 coat subunits within an icosahedral asymmetric unit

Salt bridges		Hydrogen bonds	
Glu3	Lys246	Thr6	Lys248
Arg35	Glu257	Thr8	Lys248
Arg159	Glu176	Gln94	Gln259
		Arg35	Ala253
		Thr6	Lys246
		Thr8	Ser250
		Gln37	Ser250
		Ile4	Tyr279
		Ile4	Phe280
		Gln94	Ala265
		Tyr5	Lys278
		Gly2	Asn281
		Gln37	Ala253
		Gln10	Lys248
		Thr6	Glu257
		Ser72	Asp245
		Ser291	Ser291
		Gln63	Ser198
		Tyr205	Gln207
		Lys185	Val239
		Lys185	Gly241
		Thr74	Pro243
		Arg240	Ala289
		Gln10	Asn20
		Asn28	Asn131
		Arg27	Gln130

The table summarizes the most frequently established salt bridges and hydrogen bonds among subunits.

Table S2. Data collection statistics for the A223 C-terminal domain X-ray structure

Dataset	A223-L208M C-terminal	A223-L208M C-terminal Pt peak	A223-L208M C-terminal Pt remote	A223-L208M C-terminal Pt Inflection
Wavelength, Å	0.95369	1.07170	0.855031	1.07196
Space group			$P3_22$	
Cell constants (a, b, c), Å	65.9	66.0	66.0	66.0
$\alpha = \beta = 90°$, $\gamma = 120°$	65.9	66.0	66.0	66.0
	43.7	43.5	43.5	43.5
Resolution range, Å	50–1.37 (1.42–1.37)	50–1.28 (1.33–1.28)	50–1.38 (1.43–1.38)	50–1.38 (1.43–1.38)
Unique reflections	21,677 (2,027)	27,058 (2,577)	21,189 (2,245)	21,502 (2,238)
Average redundancy	5.9 (5.2)	11.6 (11.1)	6.1 (6.1)	5.9 (5.9)
I/σ	23.0	21.1	18.9	24.0
Completeness, %	93.0 (89.2)	94.7 (91.7)	92.7 (100)	93.9 (100)
R_{sym}*, %	2.8 (25.5)	6.4 (31.9)	5.1 (32.7)	4.5 (22.1)

Numbers in parentheses refer to the highest resolution shell.

*$R_{sym} = 100 \times \Sigma_h\Sigma_i|I_i(h) - \langle I(h)\rangle|/\Sigma_h I(h)$ where $I_i(h)$ is the i^{th} measurement of reflection h and $\langle I(h)\rangle$ is the average value of the reflection intensity. Pt, platinum.

Table S3. Refinement statistics for the A223 C-terminal domain X-ray structure

Resolution, Å	19.34–1.40
No. of reflections	19,450
R_{work}/ R_{free}	13.21/15.79
No. of atoms	848
rmsd	
Bond lengths, Å	0.028
Bond angles, °	2.38
MOLPROBITY scores	
All-atom clashscore (percentile)	0.8
Bad rotamers, %	0
Ramachandran outliers, %	0
Ramachandran favored, %	98.8
MOLPROBITY score, percentile	100